INTERNATIONAL JOURNAL FOR NUMERICAL AND ANALYTICAL METHODS IN GEOMECHANICS
Int. J. Numer. Anal. Meth. Geomech., 2005; **29**:141–162
Published online in Wiley InterScience (www.interscience.wiley.com). DOI: 10.1002/nag.408

Indentation of a free-falling lance penetrometer into a poroelastic seabed

Derek Elsworth*,† and Dae Sung Lee

Department of Energy and Geo-Environmental Engineering, Pennsylvania State University, University Park, PA 16802-5000, U.S.A.

SUMMARY

A solution is developed for the build-up, steady and post-arrest dissipative pore fluid pressure fields that develop around a blunt penetrometer that self-embeds from freefall into the seabed. Arrest from freefall considers deceleration under undrained conditions in a purely cohesive soil, with constant shear strength with depth. The resulting decelerating velocity field is controlled by soil strength, geometric bearing capacity factors, and inertial components. At low impact velocities the embedment process is controlled by soil strength, and at high velocities by inertia. With the deceleration defined, a solution is evaluated for a point normal dislocation penetrating in a poroelastic medium with a prescribed decelerating velocity. Dynamic steady pressures, P_D, develop relative to the penetrating tip geometry with their distribution conditioned by the non-dimensional penetration rate, U_D, incorporating impacting penetration rate, consolidation coefficient and penetrometer radius, and the non-dimensional strength, N_D, additionally incorporating undrained shear strength of the sediment. Pore pressures develop to a steady peak magnitude at the penetrometer tip, and drop as $P_D = 1/x_D$ with distance x_D behind the tip and along the shaft. Peak induced pressure magnitudes may be correlated with sediment permeabilities, post-arrest dissipation rates may be correlated with consolidation coefficients, and depths of penetration may be correlated with shear strengths. Together, these records enable strength and transport parameters to be recovered from lance penetrometer data. Penetrometer data recorded off La Palma in the Canary Islands (*J. Volcanol. Geotherm. Res.* 2000; **101**:253) are used to recover permeabilities and consolidation coefficients from peak pressure and dissipation response, respectively. Copyright © 2004 John Wiley & Sons, Ltd.

KEY WORDS: PUPPI penetrometer; permeability; CPT; dislocation

1. INTRODUCTION

Tethered and untethered penetrometers have been used for the determination of seabed [1] and lakebed [2, 3] characteristics. Of prime interest here is the determination of fluid, mass (chemical) and thermal fluxes on continental margins and in abyssal sediments [4], with ancillary interest in strength parameters that define stability against submarine slope failure [5]. Mass, chemical and thermal fluxes may be evaluated from differential fluid pressures, species concentrations or

*Correspondence to: D. Elsworth, Department of Energy and Geo-Environmental Engineering, Pennsylvania State University, University Park, PA 16802-5000, U.S.A.
†E-mail: elsworth@psu.edu

Received 15 November 2001
Revised 22 October 2002; 16 April 2004

temperatures with depth along the embedded lance axis; these data must be combined with Darcy's, Fick's or Fourier's laws, respectively. Implicit in the evaluation of fluxes is the assumption that permeability of the sediments may be independently defined.

Current methods of determining the permeability of the penetrated sediments involve first evaluating hydraulic diffusivity from the dissipation rate of the penetration-induced pore fluid pressures [6–10]. This requires that the strain field around the penetrometer is defined by analytical [11–14] or numerical [15–17] methods, and pore pressures estimated by coupling with an appropriate constitutive model [18, 19]. Permeability may be subsequently determined if the drained deformation modulus [8, 10] may be recovered from laboratory testing of recovered sediment samples, or in some cases from the reduction of tidally induced pore fluid pressures [20–22].

Alternatively, the use of maximum pore pressure magnitudes developed during penetrometer insertion provide a one-step method to determine permeability magnitudes in homogeneous [23, 24] or layered [32] media. This procedure offers the potential to provide independent corroboration of permeabilities where they are determined by other means, and permeability magnitudes where they are otherwise unavailable.

The following addresses this complex problem [33] by evaluating penetration-induced pore pressures around the decelerating probe. This is evaluated in two steps; first the rate of deceleration of the lance as it impacts the soft seabed is determined, and this is then used to evaluate the resulting pore pressure distributions that develop around the embedding tip and shaft.

2. EMBEDMENT DECELERATION

Consider a thin lance falling through the water column that has reached terminal velocity, U_0, and subsequently impacts the soft sediments of the seabed, as illustrated in Figure 1. These soft sediments are assumed cohesive only, and in the timeframe of deceleration of the lance, behave as undrained, for the purposes of this first evaluation. The undrained cohesive strength, S_u, is assumed constant with depth, and the lance is sufficiently long that the tip-region is short in comparison with overall length of the penetrometer. Where strength is linearly varying, an average strength magnitude representative of the depth profile may be substituted. As the lance tip, assumed blunt in this analysis, embeds within the soil, to a distance x' below the seabed surface, the force resisting embedment builds. The bearing capacity, q_u, of the lance may be defined in terms of the end-bearing area, A_p, and shaft area, A_s, as

$$q_u = A_p(S_u N_c + \sigma_{v0}) + A_s S_u \tag{1}$$

where σ_{v0} is the total stress, absent the sea pressure, at current tip embedment-depth, x', and N_c is the non-dimensional bearing capacity factor, typically approaching 9 for depth to diameter ratios greater than 4.5 [25]. The rightmost two terms of stress and shaft friction vary linearly with embedment depth, x', and Equation (1) may be redefined as

$$q_u = A_p S_u N_c + (A_p \gamma_s + 2\pi a S_u) x' \tag{2}$$

where the probe diameter is $2a$, and γ_s is the buoyant unit weight of the soil. Alternatively, the bearing force, acting in the direction of negative x', may be defined as a linear function of

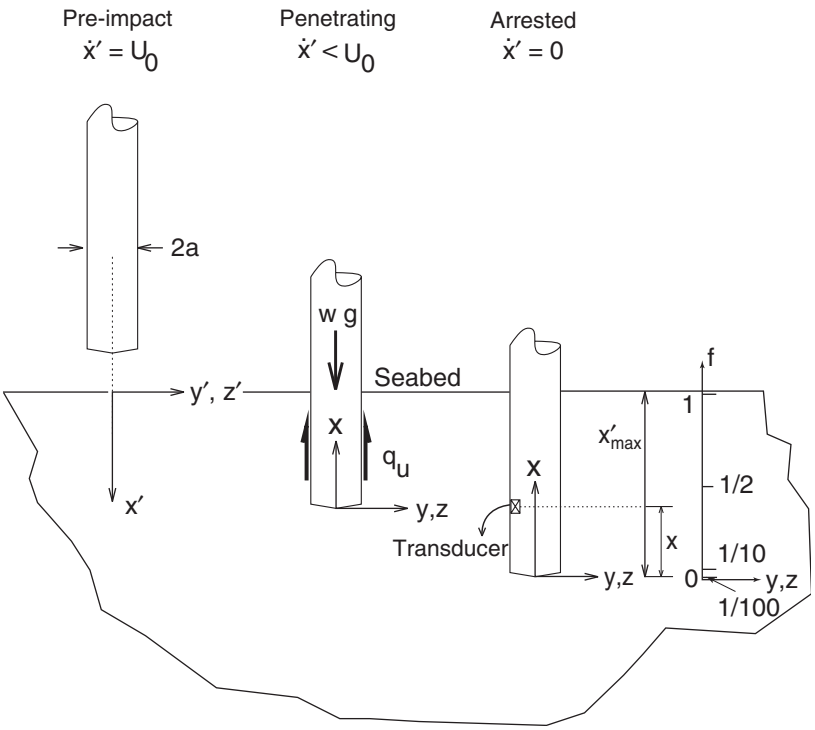

Figure 1. Schematic of a lance falling at terminal velocity, U_0, and impacting the seabed. For embedment, the co-ordinate system is fixed to the seafloor as the lance self-embeds under undrained conditions. For the evolving partially drained analysis of embedment-generated pore pressures, the co-ordinate system is fixed to the penetrometer tip.

depth as

$$q_u = N'_c + N'_q x' \tag{3}$$

with $N'_c = A_p S_u N_c$ and $N'_q = A_p \gamma_s + 2\pi a S_u$. This enables a force balance to be completed on the free-falling penetrometer as it embeds in the seabed, and the end-bearing force builds linearly with embedment. Balancing the vertically downward absolute mass, w, and buoyant mass, w_b of the penetrometer with the vertically upward resistance, q_u, of the combined end- and shaft-resistance, yields, when balanced with inertial force,

$$w\ddot{x}'[t] = w_b g - N'_c - N'_q x'[t] \tag{4}$$

The double overdot represents acceleration. The lance is rigid, and translates with the motion of the tip, indexed in this relation as x'. Pressure drag and viscous drag forces of the penetrometer in water are neglected—rather we prescribe the terminal velocity of the probe, U_0. As the probe transits from water to the seabed, this discontinuous transition is accommodated by the building resistance of the soil, through N'_c and N'_q. The initial conditions are set at time $t = 0$ when the lance-tip first impacts the seabed at velocity, U_0, as

$$\begin{aligned} x'[t=0] &= 0 \\ \dot{x}'[t=0] &= U_0 \end{aligned} \tag{5}$$

Solving the differential equation (4) for the boundary conditions of Equation (5) enables the progress of embedment with time to be defined as (see appendix for details)

$$\dot{x}'[t] = U_0 \cos\left[\sqrt{\frac{N'_q}{w}}t\right] = U \tag{6}$$

for velocity, and

$$x'[t] = U_0\sqrt{\frac{w}{N'_q}}\sin\left[\sqrt{\frac{N'_q}{w}}t\right] \tag{7}$$

for embedment depth, where $b = \sqrt{N'_q/w}$. These relations may be used to evaluate the development of pore fluid pressures that result from penetration, where the requirement for undrained penetration is relaxed. Pore pressures generated around the decelerating probe may be determined from the approximate probe velocity as the unit decelerates.

3. DISLOCATION ANALYSIS

The velocity of penetration is defined by the previous total stress analysis using the undrained strength parameters. The resulting pore pressures generated around the penetrometer shaft, and their subsequent dissipation, are evaluated by an effective stress analysis. This is an accepted method of simplifying complex behaviours [26]. Since the duration of penetrometer insertion will be of the order of a few seconds, and the time for dissipation generally of the order of minutes to days, this overlap in time is not serious. Since the resistance to insertion is defined purely in terms of undrained cohesive strength, the insertion deceleration and subsequent response will not be reliably determined where significant drainage occurs concurrent with insertion.

The behaviour of a sharp penetrometer, moving within a poroelastic medium, may be represented by a moving volumetric dislocation. The incremental form of this is a point volumetric dislocation, of volume $\mathrm{d}V$ (L^3), representing the dilation in unit time, t, subjected to a volumetric dilation rate, $v(L^3T^{-1})$, as $\mathrm{d}V = v\,\mathrm{d}t$. For $t \geqslant 0$ a volumetric dislocation is introduced at the origin ($x = y = z = 0$) with the poroelastic medium moving at velocity $+U$ in the x-direction of the fixed Cartesian co-ordinate system, representing a dislocation migrating within an infinite medium, as illustrated in Figure 1. The velocity of migration is $U = U_0\cos[bt]$, and the location at time, t, is $x'[t] = U_0/b\sin[bt]$, where $b = \sqrt{N'_q/w}$ as identified in Equations (2), (3) and (4). The position of a point located at (x, y, z) at time t, would have been $((x - U_0/b\sin[b[t-\tau]]), y, z)$ at time τ. This migrating co-ordinate system enables the behaviour to be defined for a static dislocation [27, 28].

$$p - p_s = \frac{c\,\mathrm{d}V}{4\pi R^3}\frac{\mu}{k}\frac{\bar{\xi}^3}{2\sqrt{\pi}}\mathrm{e}^{-\bar{\xi}^2/4} \tag{8}$$

with $\bar{\xi} = \bar{R}/\sqrt{c(t-\tau)}$ and $\bar{R}^2 = [x - U_0/b\sin[b[t-\tau]]]^2 + y^2 + z^2$. The material properties defining the medium represent absolute pore fluid pressure, p, relative to the initial static fluid pressure, p_s, permeability, k, hydraulic diffusivity, c and dynamic viscosity of the fluid, μ. Physically, this solution represents the radially diminishing and spherically symmetric fluid

overpressure field that is developed when a volume dilation is opened at the origin (0, 0, 0). The result is identical to the pressures induced by the instantaneous injection of a volume of fluid, $\mathrm{d}V$. Substituting into Equation (8) for the incremental rate of dilation as $\mathrm{d}V = v\,\mathrm{d}\tau$, and integrating in time yields,

$$p - p_s = \int_0^t \frac{cv}{4\pi\bar{R}^3}\frac{\mu}{k}\frac{\bar{\xi}^3}{2\sqrt{\pi}}\mathrm{e}^{-\bar{\xi}^2/4}\,\mathrm{d}\tau \tag{9}$$

where v is the rate of volume change (L^3T^{-1}).

This is similar the standard result reported [28] for a penetrometer moving at constant velocity, v. To determine the form of the fluid pressure field that develops around a decelerating penetrometer, the response for a point volumetric dislocation must be distributed to represent the moving feature. Consider the blunt cylindrical tip of a penetrometer of radius, a, as illustrated in Figure 1. The projected area, $\mathrm{d}A$, of a blunt tipped penetrometer is defined as

$$\mathrm{d}A = \pi a^2 \tag{10}$$

For an incremental advance of the penetrometer of $U\,\mathrm{d}\tau$ in time $\mathrm{d}\tau$, the distribution of volume is $\mathrm{d}V = \mathrm{d}AU\,\mathrm{d}\tau$, and substituting the relation of Equation (10), and noting from the previous that $\mathrm{d}V = v\,\mathrm{d}\tau$, then,

$$v = \pi a^2 U = \pi a^2 U_0 \cos[b[t-\tau]] \tag{11}$$

This may be substituted directly into Equation (9) to yield

$$p - p_s = \frac{\mu}{k}\frac{U_0 a^2 c}{8\sqrt{\pi}}\int_0^t \frac{\tilde{\xi}^3}{\tilde{R}^3}\mathrm{e}^{-\tilde{\xi}^2/4}\cos[b(t-\tau)]\,\mathrm{d}\tau \tag{12}$$

where the tilde overbar denotes inclusion of the variable co-ordinate of integration as $\tilde{x} = x - U_0/b\sin[b[t-\tau]]$ and

$$\begin{aligned}\tilde{R} &= \sqrt{\tilde{x}^2 + y^2 + z^2}\\ \tilde{\xi} &= \frac{\tilde{R}}{\sqrt{c(t-\tau)}}\end{aligned} \tag{13}$$

representing migrating co-ordinates and a reciprocal non-dimensional time.

3.1. Mechanistic and geometric methods

The deforming medium is assumed poroelastic, and correspondingly neglects processes of failure local to the penetrometer tip. These models have been previously applied to represent the dissipation process that results around an arrested penetrometer [23]. Pressure dissipation results for dislocation models [23] fall within a narrow band of responses for cavity expansion [6] and strain path [8] methods. Cavity expansion and strain path models are shown well-suited in representing complex material models, but are incapable of accommodating partial drainage concurrent with penetration. Conversely, dislocation models represent simple material models but readily accommodate important conditions of partial drainage.

The uniformity of each of these approaches may be indexed by the time taken to reach 50% dissipation of pore fluid pressures, t_{D}^{50}, where $t_{\mathrm{D}}^{50} = 4ct/a^2$. For pressures measured at the tip, the magnitudes of t_{D}^{50}'s are 16, 4, and 2, for strain path, cavity expansion, and dislocation methods,

respectively [23]. For shaft locations, 10 radii behind the tip ($x = 10a$) the stress path and dislocation methods yield t_D^{50}'s of 1.2×10^2 and 1.5×10^2, respectively [23].

Penetration into the seabed is resisted by a combination of shaft adhesion and end-bearing. In the event that shaft adhesion cannot be sustained, for example by the development of separation during insertion, its effect may be removed. In this instance the resistance to penetration will be near constant with insertion. At lance embedment depth to diameter ratios greater than 4.5, the end bearing capacity factor, N_c, will approach 9 [25]. This corresponds to lance penetration to 180 mm (for a 40 mm diameter probe), or 10% of the penetration depth. This is readily obtained. A uniform strength is assumed with depth, although linearly increasing strength may be accommodated, resulting in a quadratically increasing resistance with penetrations depth. This case has not been evaluated, but may be approximated by choosing a constant strength that is representative of the average strength over the range of depths penetrated.

Since the solution represents penetration within an infinite medium, the influence of the free surface is not accommodated. Magnitudes of induced pore water pressures close to the mudline will not be well represented. Induced undrained pore pressures developed by the inflation of a static dislocation within a half-space [29], may be compared with the current solution, by comparing magnitudes of mean stress. The mean stresses predicted for the half-space solution, along the trajectory of the penetrometer, but for a static dilation, note a maximum error (over-estimation of pressures by the infinite solution) of less than 10% for pressures measured within one-quarter ($x_D = \frac{1}{4} U_D/N_D$) of the burial depth of the tip below the mudline. This error increases to not more than 40% for pressures measured within one-half ($x_D = \frac{1}{2} U_D/N_D$) of the burial depth of the tip. These errors will more significantly affect data reduction methods that rely on peak pressure magnitudes, than those that rely on rates of dissipation of relative pore pressure magnitudes. Rates in the latter will be little affected, and peak pore pressures measured both at the tip, and at the quarter-depth location on the probe will be little affected.

3.2. Non-dimensional parameters

The behaviour of the system may be defined in terms of the non-dimensional parameters of excess fluid pressure, P_D, penetration rate, U_D, strength, N_D, and time, t_D, as

$$P_D = \frac{4(p - p_s)}{U_0 a} \frac{k}{\mu} \tag{14}$$

$$U_D = \frac{U_0 a}{2c} \tag{15}$$

$$N_D = \frac{ba^2}{2c} \tag{16}$$

$$t_D = \frac{4ct}{a^2} \tag{17}$$

$$(x_D; y_D; z_D) = \frac{1}{a} (x; y; z) \tag{18}$$

with $\tilde{R}_D = \sqrt{\tilde{x}_D^2 + y_D^2 + z_D^2}$, $\tilde{x}_D = \tilde{x}/a$ or $\tilde{x}_D = x_D - U_D/N_D \sin[\frac{1}{2} N_D(t_D - \tau_D)]$. These parameters give, respectively, non-dimensional pressures, impact velocities, strength, time, and locations.

These non-dimensional parameters may be substituted into Equation (12) to give, in final form the behaviour around a blunt penetrometer as

$$P_{\mathrm{D}} = \frac{1}{\sqrt{\pi}} \int_0^{t_{\mathrm{D}}} \frac{\mathrm{e}^{-\tilde{R}_{\mathrm{D}}^2/(t_{\mathrm{D}}-\tau_{\mathrm{D}})}}{[t_{\mathrm{D}}-\tau_{\mathrm{D}}]^{3/2}} \cos\left[\tfrac{1}{2} N_{\mathrm{D}}(t_{\mathrm{D}}-\tau_{\mathrm{D}})\right] \mathrm{d}\tau_{\mathrm{D}} \tag{19}$$

This enables magnitudes of pore pressure build-up to be determined following initiation of penetration within an infinite medium. Application to this is described in the following.

4. PARAMETRIC BEHAVIOUR

4.1. Post-initiation pressure build-up

The non-dimensional pressure, P_{D}, defined in Equation (19), may be used to define the build-up of pressure following the impact of the penetrometer with the surface of the seabed. The penetrometer impacts the seabed at velocity U_0, represented in dimensionless magnitude as U_{D}, and decelerates to arrest. Both the length of embedment at arrest, and the time to arrest may be evaluated from Equations (A9). The instant of impact is taken as time $t = 0$, when the velocity is U_0, enabling the time to arrest to be defined in non-dimensional terms as, $t'_{\mathrm{D}} = \pi/N_{\mathrm{D}}$. At this time, the embedment depth is a maximum, with the seabed present to a height of $x'_{\mathrm{D}}\mathrm{maximum} = U_{\mathrm{D}}/N_{\mathrm{D}}$ along the shaft. For steady penetration, the peak magnitude of dimensionless pressure is defined as $P_{\mathrm{D}} = (1/R_{\mathrm{D}})\mathrm{e}^{-U_{\mathrm{D}}(R_{\mathrm{D}}-x_{\mathrm{D}})}$ [28], which for locations on the shaft ($R_{\mathrm{D}} = x_{\mathrm{D}}$) asymptotes to $P_{\mathrm{D}}x_{\mathrm{D}} = 1$. This normalizing parameter is used in the representation of normalized pressure data in the following parametric investigation.

Pressure build-up response may be evaluated over the period from impact to arrest, for $0 < t_{\mathrm{D}} < t'_{\mathrm{D}}$, and for a variety of impact velocities and material strengths. Impact velocity is represented by U_{D}, and material strength by N_{D}. For soft seabed clays with undrained strength, S_u, of the order of 10–50 kN/m^2, magnitudes of N_{D} are in the range 1–1000. It is convenient to compare the build-up of pore pressures with respect to a given location of the transducer at x_{D}. To make comparisons feasible, we choose the transducer location with respect to the embedment depth, $N_{\mathrm{D}}/U_{\mathrm{D}}$. Correspondingly, Figure 2(a) represents the pressure build-up for the transducer placed one-half of the distance back from the penetrometer tip, or one-half of the distance from the seabed, at full embedment. Axes of the figure are selected that take advantage of the known behavior of pressure build-up. Non-dimensional pressures are plotted as the product $P_{\mathrm{D}}x_{\mathrm{D}}$, since it is known that the peak pressures, shown in this format asymptote to unity, as $P_{\mathrm{D}}x_{\mathrm{D}} \to 1$. Time is reported as $t_{\mathrm{D}}N_{\mathrm{D}}/\pi$, since we know that arrest occurs at $t'_{\mathrm{D}} = \pi/N_{\mathrm{D}}$, hence arrest occurs at $t_{\mathrm{D}}N_{\mathrm{D}}/\pi = 1$.

Apparent from Figure 2(a) is that at very high impact velocities, with $U_{\mathrm{D}} \geqslant 10^1$, the pressure response is rapid and corresponds to $t_{\mathrm{D}}N_{\mathrm{D}}/\pi = 2/\pi \arcsin[x/x'_{\mathrm{maximum}}]$, where x'_{maximum} is the embedment length at arrest, and x is the location of the pressure transducer behind the penetrometer tip. This can be alternately reported with $x/x'_{\mathrm{maximum}} = 1/f$ where $1/f$ is the proportion of the embedment length that denotes the transducer location. This represents the time that the transducer enters the sharply defined pressure bulb created by the penetrometer as it enters the seabed. For Figure 2(a) this time is represented by $t_{\mathrm{D}}N_{\mathrm{D}}/\pi = \frac{1}{3}$.

For slower impact velocities, the pressure build-up is given by the series of parallel curves, each offset by two orders-of-magnitude in dimensionless time, or one order-of-magnitude in

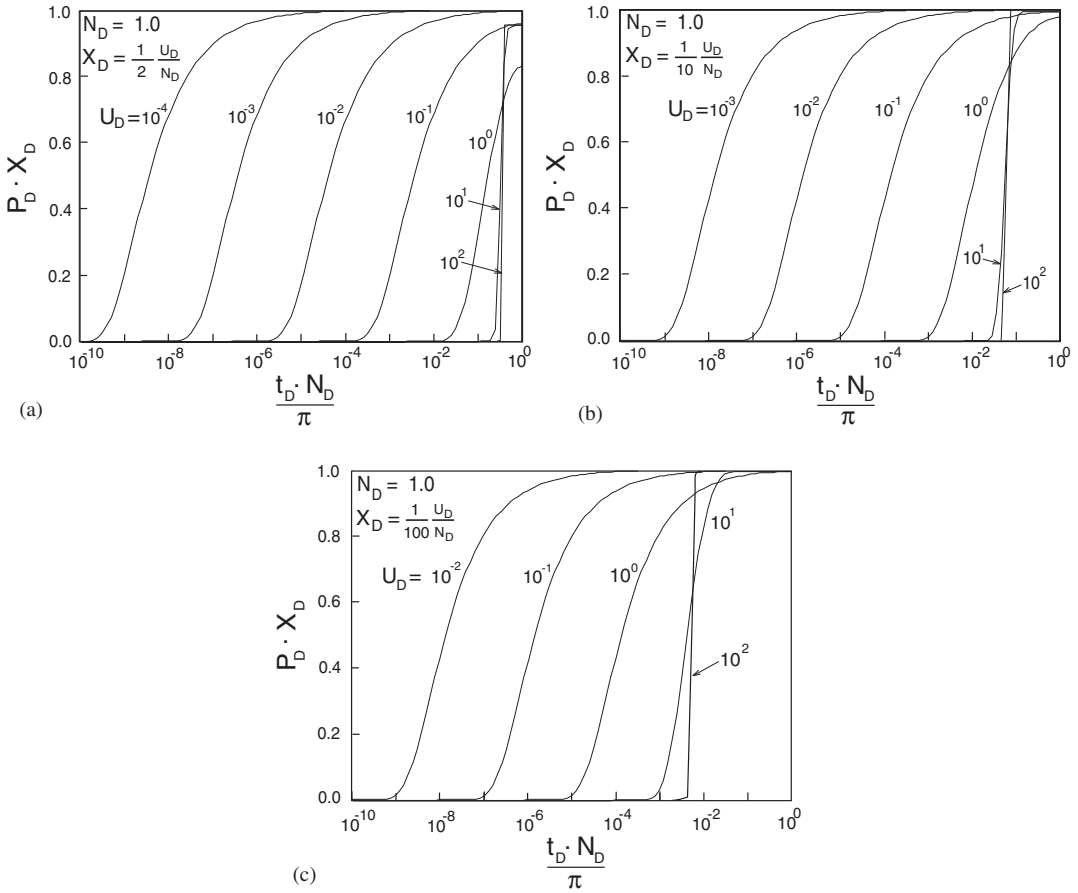

Figure 2. Build-up of non-dimensional pressure, $P_D x_D$, with time, $t_D N_D/\pi$, for a selected pressure monitoring location on the penetrometer shaft, at ordinate (a) $x_D = \frac{1}{2} U_D/N_D$; (b) $x_D = \frac{1}{10} U_D/N_D$; and (c) $x_D = \frac{1}{100} U_D/N_D$; behind the penetrometer tip. This represents a proportional length of $\frac{1}{2}$, $\frac{1}{10}$ or $\frac{1}{100}$ of the final embedment length behind the penetrometer tip. Pressure response is for impact at various velocities, U_D.

dimensionless root-time. For a given impact velocity, U_0, the magnitude of U_D decreases by one order-of-magnitude with an increase in permeability of one order of-magnitude, and non-dimensional time also increases by one order-of-magnitude. Hence, if Figure 2(a) is alternatively replotted with the ordinate as $t_D N_D/\pi U_D^2$, as shown in Figure 3(a), the response for all slow impacts overprint as a single response for $U_D \leqslant 10^{-1}$, and the rapid impact behaviour shows increasingly rapid response time.

As the pressure monitoring location is moved close to the tip as one-tenth of the embedment depth ($x_D = \frac{1}{10} U_D/N_D$) and one-hundredth of the embedment depth ($x_D = \frac{1}{100} U_D/N_D$) as illustrated in Figures 2(b) and (c), the diffusive response is shifted in time. This represents a quicker response to reach steady state, relative to time to arrest as permeability increases. In

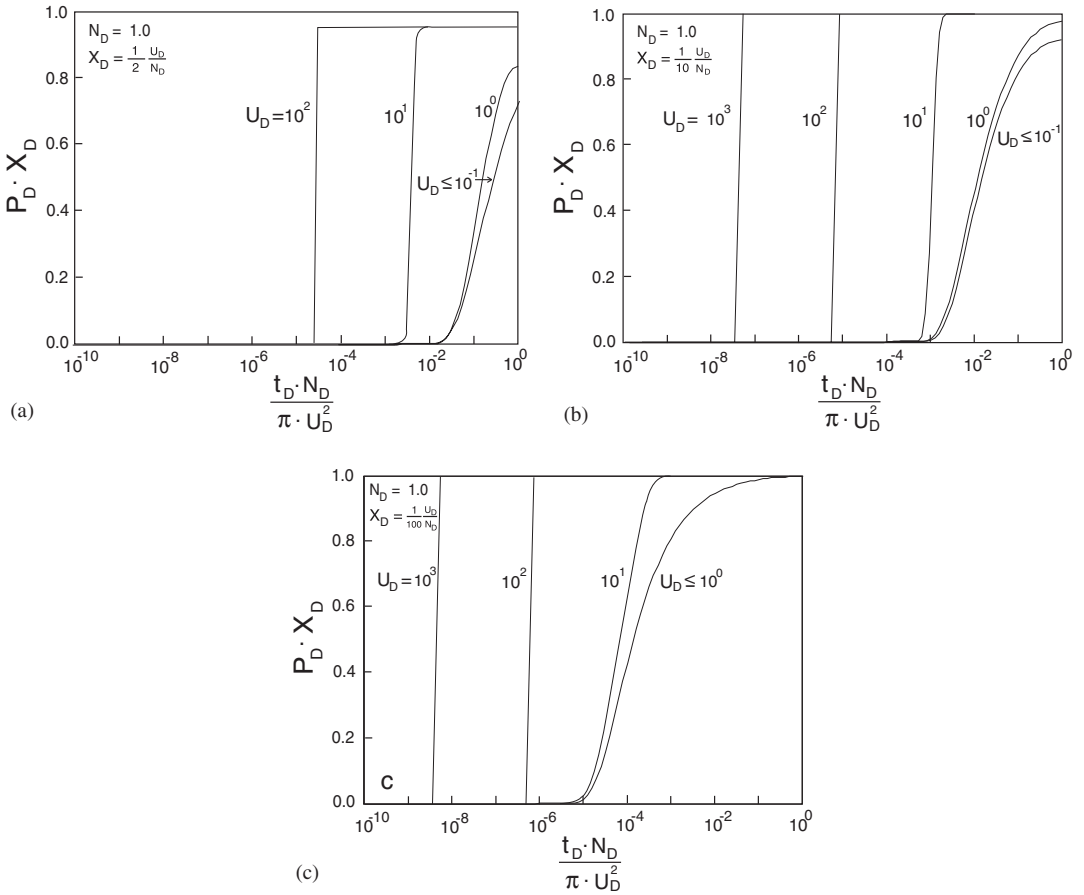

Figure 3. Build-up of non-dimensional pressure, $P_D x_D$, with time, $t_D N_D/\pi U_D^2$, for a selected pressure monitoring location on the penetrometer shaft, at ordinate (a) $x_D = \frac{1}{2} U_D/N_D$; (b) $x_D = \frac{1}{10} U_D/N_D$; and (c) $x_D = \frac{1}{100} U_D/N_D$; behind the penetrometer tip. Pressure response is for impact at various velocities, U_D.

Figure 2(b) and (c) the diffusive response is merely shifted in time by two orders-of-magnitude for a one order-of-magnitude increase in permeability, and hence, U_D. For the pressure build-up due to the transducer moving into the pressure bulb, generated instantaneously with insertion, the asymptotic values of $t_D N_D/\pi$ are 0.064 and 0.0064 for the probes with a transducer one-tenth ($1/f = \frac{1}{10}$ in Figure 2(b)) and one-hundredth ($1/f = \frac{1}{100}$ in Figure 2(c)) of the embedment length from the tip, respectively. This behavior is also apparent for the modified ordinates of Figures 3(b) and (c).

4.2. Peak pressure magnitudes

Unlike penetration at constant velocity, U, where the pressures build to a dynamic steady state [28] the peak pressures of interest for the decelerating penetrometer, occur at the time of

penetrometer arrest. From this state the pressures then dissipate. The distribution of peak pressures on the shaft of a decelerating penetrometer may be determined from $t|_{\dot{x}'=0}$, defined in equation (A5), and resubstituted into equation (19), as $t'_{\mathrm{D}} = \pi/N_{\mathrm{D}}$. Since the penetrometer may arrest before it reaches a steady pressure distribution, it is likely that the pressure induced around a decelerating penetrometer may, in some circumstances, be less than for steady penetration.

The steady pressure distribution around a blunt penetrometer under constant velocity penetration of U, is defined as [28]

$$P_{\mathrm{D}} = \frac{1}{R_{\mathrm{D}}} \mathrm{e}^{-U_{\mathrm{D}}(R_{\mathrm{D}} - x_{\mathrm{D}})} \tag{20}$$

where the non-dimensional penetration velocity is $U_{\mathrm{D}} = Ua/2c$. Behind the blunt tip of the penetrometer, and on the shaft, this reduces to $P_{\mathrm{D}} = 1/x_{\mathrm{D}}$, allowing direct comparison with peak pressure magnitudes for the decelerating penetrometer. Most conveniently, this is plotted as $\log x_{\mathrm{D}}$ versus $\log P_{\mathrm{D}}$, where Equation (20) plots as a straight line, as apparent in Figure 4. For a decelerating penetrometer, the results asymptote to the distribution defined for $U_{\mathrm{D}} \leqslant 10^{-1}$ for slow impact. Under these conditions the pore pressure distribution around the tip has not reached the dynamic steady state represented by the straight line for $P_{\mathrm{D}} = 1/x_{\mathrm{D}}$. The pressure distribution for slow penetration will be near-spherical around the tip, and is influenced by the aggregate velocity along the path of the penetrometer, terminating at zero velocity.

Where the penetrometer impacts at a higher velocity, for example for $U_{\mathrm{D}} \geqslant 10^{0}$, the pressure distribution asymptotes to the steady behaviour. As non-dimensional impact velocities become larger, the match to the steady behaviour becomes closer, mainly because the embedment length increases proportionally to U_{D} as $x'_{\mathrm{D}} = U_{\mathrm{D}}/N_{\mathrm{D}}$. These curves will be self-similar as the

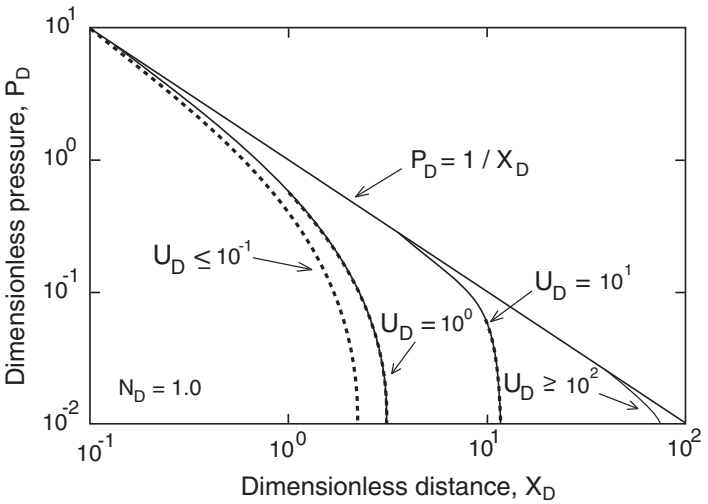

Figure 4. Peak dimensionless pressure, P_{D}, measured along the penetrometer shaft, at location x_{D}, at the time of penetrometer arrest, $t'_{\mathrm{D}} = \pi/N_{\mathrm{D}}$. All pressures are for a blunt penetrometer with the sediment characterized by a dimensionless strength of $N_{\mathrm{D}} = 1$. Data for measuring locations stranded above mudline are shown by dashed line.

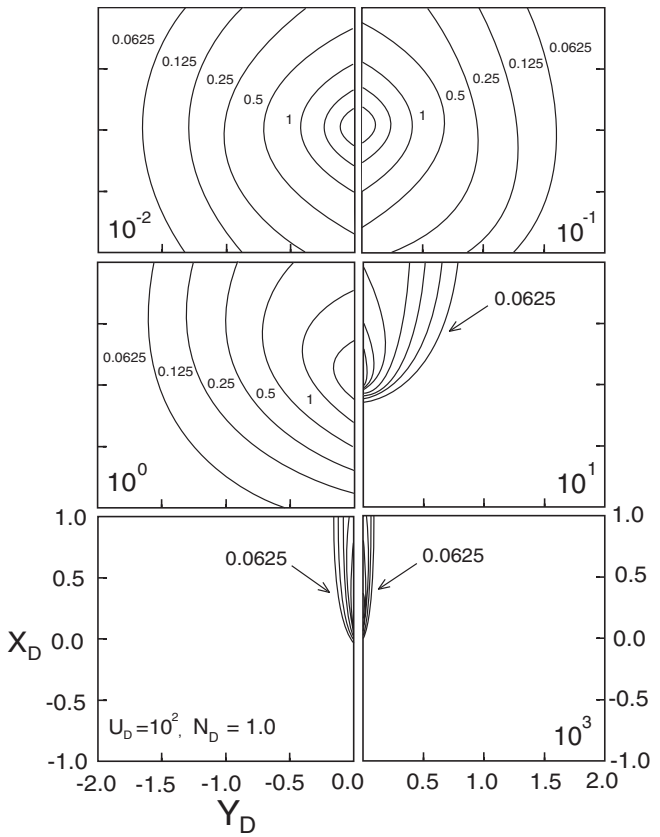

Figure 5. Peak pressure distribution centered on the tip of a blunt penetrometer at $(x_D, y_D) = (0, 0)$. Results document magnitudes of P_D in multiples of 2^{-n} within a radius of $R'_D = 1$ of the cone tip. All figures locate the tip at the time of arrest, at the origin of the plot.

embedment length increases. Note that the pressure distributions are not truncated at the seabed, for $x_D > U_D/N_D$, because the medium is considered infinite, rather than semi-infinite, even though the effect of penetration is only applied following the presumed impact at the seabed at velocity U_0. As discussed previously, this effect will be small for typical embedment length.

The form of the contoured distribution of pressures around the tip is shown in Figure 5. For high velocity impacts, the pressure distribution is cylindrical around the penetrometer, and markedly decreases in spread away from the penetrometer with an increase in non-dimensional impact velocity, U_D. As the impact velocity is reduced, the pressure distribution becomes spherical, representing the dominant influence of the most recent portion of the advancing penetrometer, local to the tip. As non-dimensional impact velocities are reduced below $U_D < 10^{-1}$, the distributions become identical, indicating the control of pressure diffusion in dissipating the pressures, and a reduction in the relative influence of the migrating penetrometer. Importantly, the contoured representations are not truncated at the seabed

surface, as the diffusive solution is for an infinite medium, even though the penetrometer was only 'turned-on' as it impacted the seabed surface.

4.3. Post-arrest

Behaviour, post-arrest may be evaluated by superposing a moving dislocation of negative strength, beginning at the time of arrest, $t|_{x'=0}$, defined as t'_{D}, over the non-arrested moving dislocation. Physically, the dislocation represents the insertion of the steel lance into the seabed. Rather than arresting the penetrometer, a more convenient mathematical construct is to allow the lance to continue on its trajectory. A concurrent and colinear lance shadows it, but of opposite sense and is turned-on only at the time of arrest. A dilation plus a colocated contraction exactly cancel each other, resulting in a null effect. Behavior at any time, $t_{\mathrm{D}} > t'_{\mathrm{D}}$, may be determined from the coincident and colinear moving dislocations, the first representing dilation from $0 \rightarrow t_{\mathrm{D}}$ and the second representing an equivalent but opposite contractile volumetric dislocation from $t'_{\mathrm{D}} \rightarrow t_{\mathrm{D}}$ beginning from the location of the arrested tip at time t'_{D}. The system of equations follow directly from Equation (19) as

$$P_{\mathrm{D}} = \frac{1}{\sqrt{\pi}} \int_0^{t_{\mathrm{D}}} \frac{\mathrm{e}^{-\tilde{R}_{\mathrm{D}}^2/(t_{\mathrm{D}}-\tau_{\mathrm{D}})}}{[t_{\mathrm{D}}-\tau_{\mathrm{D}}]^{3/2}} \cos\left[\tfrac{1}{2} N_{\mathrm{D}}(t_{\mathrm{D}}-\tau_{\mathrm{D}})\right] \mathrm{d}\tau_{\mathrm{D}} - \frac{1}{\sqrt{\pi}} \int_{t'_{\mathrm{D}}}^{t_{\mathrm{D}}} \frac{\mathrm{e}^{-\tilde{R}_{\mathrm{D}}^2/(t_{\mathrm{D}}-\tau_{\mathrm{D}})}}{[t_{\mathrm{D}}-\tau_{\mathrm{D}}]^{3/2}} \cos\left[\tfrac{1}{2} N_{\mathrm{D}}(t_{\mathrm{D}}-\tau_{\mathrm{D}})\right] \mathrm{d}\tau_{\mathrm{D}} \tag{21}$$

or alternatively as

$$P_{\mathrm{D}} = \frac{1}{\sqrt{\pi}} \int_0^{t'_{\mathrm{D}}} \frac{\mathrm{e}^{-\tilde{R}_{\mathrm{D}}^2/(t_{\mathrm{D}}-\tau_{\mathrm{D}})}}{[t_{\mathrm{D}}-\tau_{\mathrm{D}}]^{3/2}} \cos\left[\tfrac{1}{2} N_{\mathrm{D}}(t_{\mathrm{D}}-\tau_{\mathrm{D}})\right] \mathrm{d}\tau_{\mathrm{D}} \tag{22}$$

where the co-ordinate system migrates with the continuously migrating dislocation, post-arrest, and pressures are referenced relative to this co-ordinate system. To transform to co-ordinates relative to the arrested penetrometer, a periodic transformation must be applied. Where the co-ordinate system $[\hat{x}, \hat{y}, \hat{z}]$ is chosen to represent locations relative to the arrested penetrometer ($[\hat{x}]$ is the distance of the pressure-measuring transducer behind the penetrometer tip), the linkage between the two co-ordinate systems are

$$\begin{aligned} x &= \hat{x} - \frac{U_0}{b} + \frac{U_0}{b} \sin[b(t)] \\ y &= \hat{y} \\ z &= \hat{z} \end{aligned} \tag{23}$$

where arrest always occurs at time, $t_{\mathrm{arrest}} = t' = \pi/2b$ and

$$\tilde{x} = x - \frac{U_0}{b} \sin[b(t-\tau)] \tag{24}$$

The same non-dimensional co-ordinate system may be invoked, to yield the co-ordinate transform

$$x_{\mathrm{D}} = \hat{x}_{\mathrm{D}} - \frac{U_{\mathrm{D}}}{N_{\mathrm{D}}}\left[1 - \sin\left[\tfrac{1}{2} N_{\mathrm{D}} t_{\mathrm{D}}\right]\right] \tag{25}$$

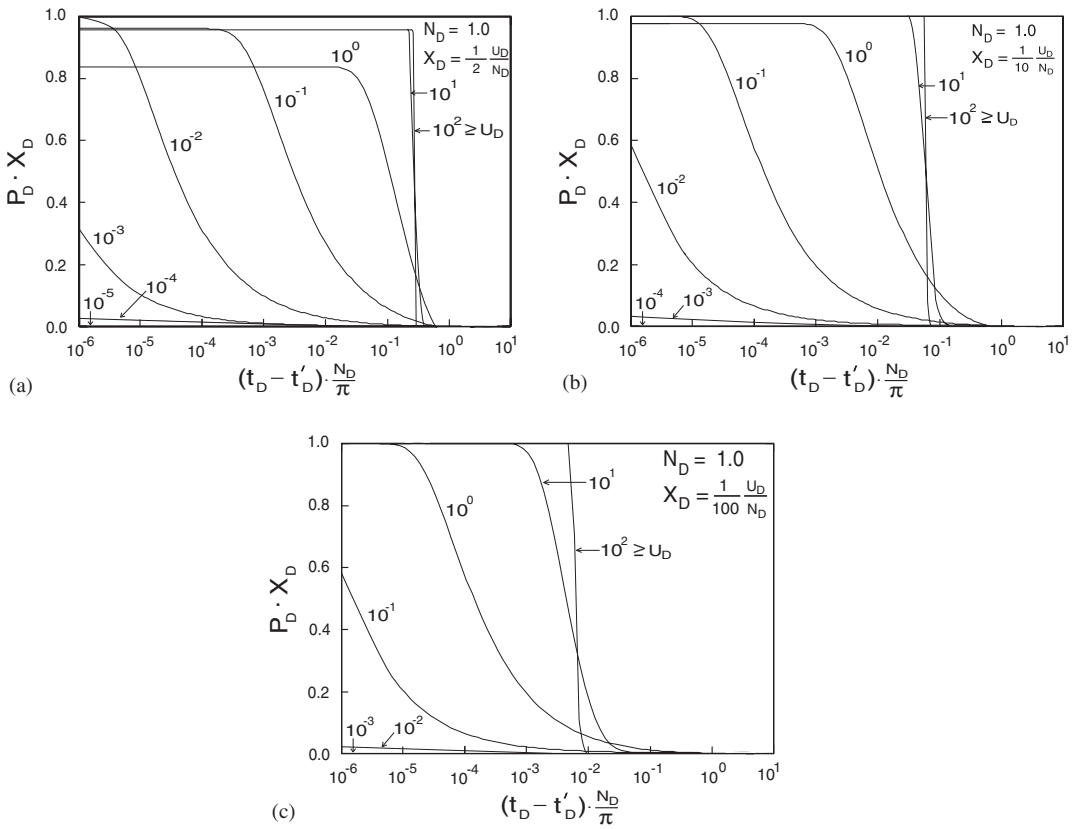

Figure 6. Dissipation response following penetrometer arrest at time, t'_D. Change in non-dimensional pressure is recorded as the product $P_D x_D$, for $N_D = 1$ and for the transducer located a distance (a) $x_D = \frac{1}{2} U_D/N_D$; (b) $x_D = \frac{1}{10} U_D/N_D$; and (c) $x_D = \frac{1}{100} U_D/N_D$, behind the penetrometer tip. This represents a constant proportion of $\frac{1}{2}$, $\frac{1}{10}$, or $\frac{1}{100}$ of the total embedment length back from the tip.

or $\tilde{x}_D = \hat{x}_D + U_D/N_D[\sin[\frac{1}{2} N_D t_D] - 1] - U_D/N_D \sin[\frac{1}{2} N_D[t_D - \tau_D]]$ by substituting Equation (25) into $\tilde{R}_D = \sqrt{\tilde{x}_D^2 + y_D^2 + z_D^2}$ yields for Equation (24) where the time to arrest is $t'_D = \pi/N_D$ and enables equation (21) to be directly evaluated.

Figures 6 describes the dissipation behaviour following arrest at time t'_D. The time since arrest is defined as $(t_D - t'_D)$, and these plots, for transducer locations at $\frac{1}{2}$, $\frac{1}{10}$ and $\frac{1}{100}$th of the embedment length from the tip follow directly from the build-up data of Figure 2. Maximum magnitudes of $P_D x_D$ track across from the build-up curves, setting the peak pressure that falls following arrest. The dissipation behaviour is included in Figure 6(a) for a pressure transducer located one-half of the embedment length back from the penetrometer tip. Similar to the pressure build-up behaviour, dissipation is rapid for low non-dimensional impact velocities, and slow for higher impact velocities. As the pressure transducer is moved closer to the penetrometer tip, as in Figure 6(b) and (c), the pore pressures have a greater opportunity to build to the steady magnitude of $P_D x_D = 1$.

The starting magnitudes for the pressures in Figure 6, are the same pressures recorded at the termination of penetration that are represented in Figure 2. Thus, the pressure trace for $U_D = 10^0$ in Figure 6(a) is a direct continuation for $P_D x_D$ in Figure 2(a). However, since Figures 6 is shown with the logarithm of time, the beginning location is not directly at the cessation of penetration ($t_D - t'_D = 0$), but some time after it, when some traces have already partially dissipated (e.g. for $U_D = 10^{-1}$ in Figure 6(c)).

At low magnitudes of non-dimensional penetration velocity, $U_D < 10^0$, the dissipation curves are all of similar form. At high impact velocities, $U_D \geqslant 10^1$, the dissipation response is rapid and results from the thin pressure 'skin' that develops around the penetrometer shaft (Figure 5). The rapid dissipation profile develops at $(t_D - t'_D)N_D/\pi = 2/\pi \arcsin[x/x'_{\text{maximum}}]$, as apparent in Figure 6(a)–(c). These results enable the time to 50% pressure dissipation, t_{50}, to be determined, enabling hydraulic diffusivity, or consolidation coefficient, c, to be determined from the dissipation response.

5. DATA ANALYSIS

For build-up behaviour, the generalized response is shown in Figure 7(a). For low penetration velocities, the build-up, for multiple N_D, is given if pressure curves are developed relative to a non-dimensioned time $t_D N_D^2/\pi f^2$, where f represents the location of the transducer relative to the tip, as $1/f = x/x'_{\text{maximum}}$. These pressure responses are correct for multiple magnitudes of N_D, and geometry, f, and are applicable for $U_D \leqslant 10^0$. As penetration rate increases, the build-up response is near instantaneous, and is given by $t_D N_D/\pi = 2/\pi \arcsin[1/f]$. Correspondingly, Figure 7(a) represents a full suite of pressure responses. This figure enables the build-up response to be evaluated, although the build-up response may be truncated at $t_D N_D/\pi = 1$, correspondingly to the time of arrest.

If the time of arrest is known, the peak pressure magnitude, corresponding to that time may be defined. In the limit, $P_D x_D = 1$, and confirms the $P_D = 1/x_D$ pressure distribution along the shaft, apparent for steady penetration, as in Equation (20). Secondly, since the non-dimensional pressure, P_D, includes the magnitude of permeability, k, the peak generated pressure may be used to evaluate transport parameters. From the definition of dimensionless pressure, P_D, of Equation (14), permeability may be determined for peak insertion pressure, $p - p_s$, as

$$\frac{k}{\mu} = \frac{U_0 a}{4(p - p_s)x_D} \tag{26}$$

provided behaviour has asymptoted to $P_D x_D = 1$. The appropriateness of using $P_D x_D = 1$ as a method of evaluating permeability, may be determined from dissipation data, used to evaluate U_D and from the form of the tip–local pressure distribution defined in Figure 5.

The generalized pressure dissipation response is included in Figure 7(b). The time-scale for this plot is different from that for pressure build-up. The slow insertion velocity response, is normalized for magnitudes of $U_D^2/N_D \leqslant 10^2$, rather than for magnitudes of U_D, as represented in Figure 7(a) for build-up. For higher penetration rates, corresponding to $U_D^2/N_D > 10^4$, the dissipation is rapid and occurs at time $(t_D - t'_D)N_D/\pi \cong 10^{-2}$. This also corresponds to the time to 50% dissipation. For the slower penetration rates, $(t_D - t'_D)_{50}/\pi N_D^2/U_D^2 = 10^{-4}$, and coefficient of consolidation may be evaluated from the time-dependent dissipation of penetration-developed pore pressures. These are determined by matching actual time–pressure

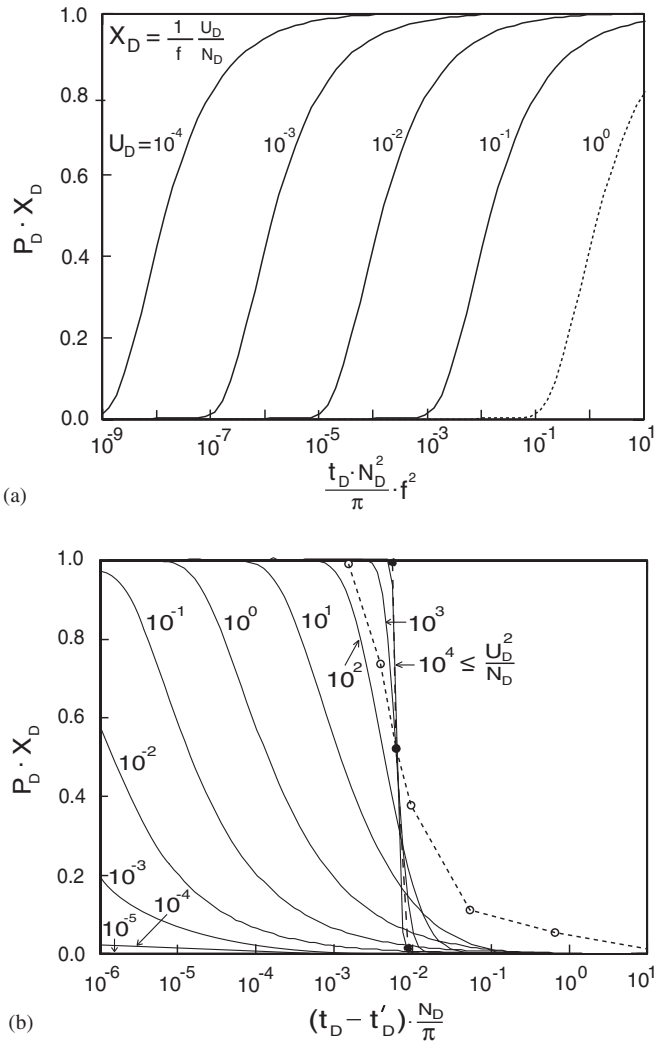

Figure 7. Generalized shaft pore pressure response in both (a) build-up, and (b) dissipation. Build-up response of (a) is for various magnitudes of soil strength, $N_D \geqslant 1$. Dotted response notes that results vary slightly with N_D for U_D approaching 10^0. Build-up for high U_D are near vertical (instantaneous) as in Figure 3, and are given by $t_D N_D/\pi = 2/\pi \arcsin[1/f]$. Dissipation response of (b) is for all N_D. Data are from [30] and represent PUPPI-2 as open circles (centred with t_{50} of 450 s), and PUPPI-4 as filled circles (centred with t_{50} of <45 s).

responses with those for dimensionless-time and dimensionless-pressure to relate time directly with diffusive time, t_D, and thereby evaluate consolidation coefficient, c.

This full suite of penetration induced pore fluid pressure and subsequent dissipation responses offer the potential to better understand tip-local processes and the determination of sediment transport parameters from recorded pore pressure response.

5.1. Data reduction

Pore pressure response from six PUPPI (Pop-up pore pressure instrument) deployments [30] off La Palma, in the Canary Islands, is available, together with geotechnical data recovered from sediment cores [31]. The PUPPI instruments comprise a thin lance with a tapered tip, capped by a ballasted instrument package. The lance may be tipped with a thinner-diameter stinger tip that extends from the main lance. The instrument may be ballasted to reach depths in excess of 6000 m. Lances are available in a variety of lengths. These are 6, 4 (50 mm diameter), or 3 (38 mm) metres, with the following data [30] gathered using the latter two types. For the 4 m probe, the ports are at 2, 3, and 4 mbsf, and for the 3 m propbe, at 1.5, 2.25, and 3 mbsf. The PUPPI deployments are co-located with the sediment sample sites, spread over about 400 km^2. Properties of the shallow cores are variable but record porosities in the range of $\sim$ 65–75%, shear strength of the order of $\sim$ 2–6 kPa with no obvious tread with depth, and water contents from $\sim$ 60 to 90%.

Standard constant-stress consolidation (oedometer) tests yield consolidation coefficients, c, in the range $\sim 3.5\text{–}8.2 \times 10^{-7}$ m^2 s^{-1}, coefficients of compressibility, m_v, 0.5–1.5 MPa^{-1}; these data enable laboratory derived permeabilities to be evaluated from $k = c \cdot m_v \cdot \mu$ as 6×10^{-16} to 6×10^{-15} m^2. Vane shear strength, s_u, to effective stress ratio, S_u/σ', in the range $\sim$ 0.5–3 in the upper 0.5 m and $\sim$ 0.2–0.5 below that denote the material as changing from overconsolidated at the seafloor, to normally consolidated below 0.5 m. The degree of overconsolidation decreases with depth, and is normally consolidated below about 1 m.

Pore pressure data from the PUPPI deployments [30] enable the evaluation of fluid transport and soil deformability parameters to be determined. The PUPPI deployments fully embed ($x_{max} = 3$ m), with $U_D \sim 10^4$. The time to 50% dissipation of excess pore pressure enables the coefficient of consolidation to be defined of the order of 10^{-6} m^2 s^{-1}. Tidal loading enables the estimation of coefficient of soil compressibility, m_v, in the range $6.2 \times 10^{-9}\text{–}1.5 \times 10^{-7}$ Pa^{-1}. These are congruent with the magnitudes evaluated from laboratory tests, and enable permeabilities to be evaluated in the range $2 \times 10^{-18}\text{–}6 \times 10^{-16}$ m^2, that span a range two orders of magnitude lower than those determined from laboratory testing.

In this work we propose that permeability magnitudes may be determined in two ways. They may be recovered from peak pressure magnitudes as a direct index of permeability, or the pressure dissipation rate may be used to define the consolidation coefficient, c, and used together with the tidally measured m_v to then obtain permeability. In the first approach we use the peak pressure data through use of Equation (26). For an impact velocity, U_0, of 0.4 m/s (impact velocity is determined from the recorded rate of pressure, measured during lance free-fall (Urgeles, personal communication)), a penetration radius, a, of 0.02 m, a location of the pressure port (x) at 1.5 m behind the tip (3 m probe), a fluid viscosity, μ, of 8.9×10^{-4} Pa s, and peak pressure ($p - p_s$) in the range, 0.4–80 kPa, permeabilities may be evaluated by substitution into Equation (26). These permeability estimates are in the range $2 \times 10^{-13}\text{–}2 \times 10^{-11}$ m^2, and are reported in Table I.

Typical insertion pressures peak at arrest, and decay exponentially to background *in situ* magnitudes over tens of minutes to a few hours [30] and are shown in general form overprinted on Figure 7(b). The narrow range of shear strength magnitudes (2–6 kPa), and broad range of peak pore pressures, spanning two orders-of-magnitude, suggest the strong influence of drainage, and thereby permeability, in controlling the insertion response.

Table I. Field transport and soil compressibility data obtained from laboratory and *in situ* testing of La Palma, Canary Islands.

Parameter	PUPPI pressure decay (Urgeles *et al.* [30])	Laboratory data (Roberts and Cramp [31])	PUPPI peak pressure* (This work)	PUPPI dissipation† (This work)
Coefficient of consolidation c [m^2 s^{-1}]	$1.3 \times 10^{-8} - 1 \times 10^{-4}$	$3.5 \times 10^{-7} - 8.2 \times 10^{-7}$	$< 7 \times 10^{-5}$	1×10^{-7}
Coefficient of soil compressibility m_v [Pa^{-1}]	$6.2 \times 10^{-9} - 1.5 \times 10^{-7}$	$5 \times 10^{-7} - 1.5 \times 10^{-6}$	—	—
Permeability k [m^2]	$2.5 \times 10^{-18} - 6.6 \times 10^{-16}$	$6 \times 10^{-16} - 6 \times 10^{-15}$	$2 \times 10^{-13} - 2 \times 10^{-11}$	$10^{-19} - 10^{-16}$

*Using the calculation sequence: permeability determined from Equation (27), and coefficient of consolidation determined from dissipation response using Figure 7(b).
†Using the calculation sequence: consolidation coefficient determinated from dissipation response using Figure 7(b), and permeability evaluated from $k = c \cdot \mu \cdot m_v$, with m_v from laboratory data.

With permeability determined from these data, coefficient of consolidation may be independently determined directly from the dissipation response. The time to 50% dissipation may be recovered from Figure 7(b). Two different responses are evident, either for $U_D^2/N_D < 10^4$, and for $U_D^2/N_D > 10^4$. Assuming first that for $U_D^2/N_D < 10^4$, then the order of magnitude separation, in time, of each of the curves yields

$$(t_D - t'_D)_{50} \frac{N_D}{\pi} \frac{N_D}{U_D^2} \cong 10^{-4} \tag{27}$$

Substituting from Equations (15)–(17) into Equation (27) yield, after rearrangement, the consolidation coefficient, c, as

$$c = \frac{U_0^2 \, \pi \, 10^{-4}}{4 \, (t - t')_{50} \, b^2} \tag{28}$$

For an impact velocity, $U_0 = 0.4$ ms^{-1}, a measured undrained shear strength of $S_u = 10$ kPa, a penetrometer mass of 50 kg, and a penetrometer radius, a, of 0.02 m, results in a magnitude of b of the order of 2.3 s^{-1}, and $U_D \sim 10^4$. A time to 50% dissipation of pore pressures $(t - t')_{50}$ of the order of 500 s [30] yields a consolidation coefficient, c, of $\sim 10^{-8}$ m^{2}s^{-1}. However, we have assumed $U_D^2/N_D < 10^4$, and must check this. Substituting the evaluated magnitude of consolidation coefficient, yields $U_D^2/N_D = 7 \times 10^6$, which violates the initial assumption $U_D^2/N_D < 10^4$. Alternatively, from Figure 7(b), note that for $U_D^2/N_D > 10^4$, then $(t_D - t'_D)_{50} N_D/\pi = 10^{-2}$, but this expression does not allow an absolute magnitude of c to be evaluated. Instead, we note that since $U_D^2/N_D > 10^4$, then substituting as before, $c < 7 \times 10^{-5}$ m^2 s^{-1}.

A second approach to determine permeabilities is to use the consolidation coefficient evaluated from insertion-pressure decay, together with the soil compressibility determined from either the tidal response [30] or from the laboratory data [31]. Using Equation (28) for $(t - t')_{50} \sim 500$ s, $U_D = 0.4$ ms^{-1}, and $b = 2.3$ s^{-1} yields a consolidation coefficient of 10^{-7} ms^{-2}, and from $k = c \; m_v \; \mu$, results in permeabilities in the range 10^{-19} m^2 (from the tidal response data) to 10^{-16} m^2 (from the laboratory test data).

Potential permeabilities span the broad range 10^{-19}–10^{-11} m^2. The highest permeabilities result from the peak pressure method, (10^{-13}–10^{-11} m^2), and are larger than the laboratory derived values (10^{-16}–10^{-15} m^2). Pressure-decay derived results are roughly congruent whether derived from static solutions (10^{-18}–10^{-16} m^2) [26, 30], or from the dynamic solution developed here (10^{-19}–10^{-16} m^2). Unfortunately the suite of results remain inconclusive. The laboratory data, absent effects of sample disturbance, should be broadly representative of behavior at the spatial scale of the size of an individual core. Permeabilities at larger spatial scales, perhaps sampled by the penetrometer-induced pressure bulb, would likely be higher than the laboratory-derived data. However, the peak pressure derived permeabilities are 2–3 orders of magnitude larger. These high permeability predictions may be conditioned by rapid pressure dissipation occasioned by the low confinement or by poor sealing along the penetrometer shaft. Conversely, large-scale permeabilities recovered from the dissipation response are considerably lower than the laboratory-derived data in the range (10^{-19}–10^{-16} m^2). That these permeabilities are lower than laboratory-derived values is more difficult to explain, although this two order-of-magnitude mismatch is fully accommodated in the stiffer large-scale modulus sampled by tidal loading, that obviates the softening effects of sampling disturbance. The difficult seafloor sampling environment makes the definitive selection of any one set of soil parameters difficult.

6. CONCLUSIONS

A theory is developed to represent the build-up and dissipation of pore pressures that result around a decelerating blunt penetrometer as it embeds within a poroelastic seabed. Pressure build-up and dissipation results have been developed for the case of a single prescribed non-dimensional strength, $N_D = 1$, and for three different monitoring locations ($x_D = \frac{1}{2} U_D/N_D$; $x_D = \frac{1}{10} U_D/N_D$; $\frac{1}{100} U_D/N_D$). This magnitude was selected as representation of lower-range seabed sediment strengths. These results may be generalized for a range of N_D values, representing various strengths, by selecting appropriate groupings of non-dimensional parameters. These parameter groups are different for build-up and for dissipation.

Although developed for nominally linear materials, the solutions provide mechanisms to evaluate transport properties of the penetrated seabed sediments. Two methods are demonstrated as feasible. The first involves the use of peak-penetration-induced pressure as a proxy for permeability—this enables the one-step evaluation of permeability, that is independent of both drained compressibility measurements on recovered cores, or correlations with tidally forced pore-fluid pressures. The second method relates the dissipation rate of pore pressures to consolidation coefficient, c. If drained soil compressibility data are available for the sediment, the permeability may be straightforwardly evaluated, as the product of consolidation coefficient, fluid viscosity, and soil compressibility. From this example data set, permeability magnitudes derived from peak pressure data are uniformly higher than those derived using pressure decay, with the latter results pre-conditioned by laboratory-derived soil compressibility data.

APPENDIX A

The equation

$$w\ddot{x}'[t] = w_b g - N'_c - N'_q x'[t] \tag{A1}$$

may be solved where initial conditions are set at time $t = 0$ when the lance-tip first impacts the seabed at velocity, U_0, as

$$\begin{aligned} x'[t=0] &= \quad 0 \\ \dot{x}'[t=0] &= U_0 \end{aligned} \tag{A2}$$

Solving the differential equation (A1) for the boundary conditions of Equation (A2) enables the progress of embedment with time to be defined as

$$x'[t] = \frac{[gw_b - N'_c]}{N'_q}\left[1 - \cos\left[\sqrt{\frac{N'_q}{w}}t\right]\right] + U_0\sqrt{\frac{w}{N'_q}}\sin\left[\sqrt{\frac{N'_q}{w}}t\right] \tag{A3}$$

and for the change in velocity, $\dot{x}'[t]$, with time as

$$\dot{x}'[t] = \frac{[gw_b - N'_c]}{N'_q}\sqrt{\frac{N'_q}{w}}\sin\left[\sqrt{\frac{N'_q}{w}}t\right] + U_0\cos\left[\sqrt{\frac{N'_q}{w}}t\right] \tag{A4}$$

In the solutions for both embedment length and velocity, the two terms represent, respectively, non-inertial penetration under self-weight (first term), and the inertial component of the lance (second term). Solving for the time until arrest is possible by setting Equation (A4) to zero as $\dot{x}'[t] = 0$ when deceleration is complete. This yields

$$t|_{\dot{x}'=0} = \sqrt{\frac{w}{N'_q}}\arctan\left[-\frac{U_0 N'_q}{[gw_b - N'_c]}\sqrt{\frac{w}{N'_q}}\right] \tag{A5}$$

for the time to arrest, or alternatively the embedment length $x'_{\max}$, as

$$x'_{\max} = \left[\frac{gw_b - N'_c}{N'_q}\right] + \left[\left[\frac{gw_b - N'_c}{N'_q}\right]^2 \cdot \frac{N'_q}{w}\frac{1}{U_0} + U_0\sqrt{\frac{w}{N'_q}}\right]\sin\left[\sqrt{\frac{N'_q}{w}}t\bigg|_{\dot{x}'=0}\right] \tag{A6}$$

This complex relation may be simplified by realizing there are two regimes of penetration; that where inertial effects are negligible, for small U_0, and alternatively where inertial effects dominate. From Equation (A4), at slow penetration velocities, as $U_0 \to 0$ then

$$U_0 \ll \frac{[gw_b - N'_c]}{N'_q}\sqrt{\frac{N'_q}{w}} \tag{A7}$$

and $t\sqrt{N'_q/w} = 0$. Substituting this into Equation (A3) yields a trivial solution of zero embedment as $x'|_{\max} = 0$. This condition is met when $N'_c \gg N'_q$, and surface bearing capacity greatly exceeds the influence of bearing at depth. The corollary to the non-inertial condition is where the impact velocity is comparatively large. For this condition,

$$U_0 \gg \frac{[gw_b - N'_c]}{N'_q}\sqrt{\frac{N'_q}{w}} \quad \text{then from Equation (A4)} \quad \sqrt{\frac{N'_q}{w}}t = \frac{\pi}{2} \tag{A8}$$

and substituting into Equation (A3) results in a maximum embedment depth of, and time to arrest of,

$$x'|_{\max} = U_0 \sqrt{\frac{w}{N'_q}} \quad \text{at time } t = \frac{\pi}{2}\sqrt{\frac{w}{N'_q}} \tag{A9}$$

The consequence of Equation (A9) is that shear strength, S_u, may be determined from either knowledge of the impact velocity and embedment length, or from knowledge of the time to decelerate to zero velocity. Each reduction method enables N'_q to be determined, and hence S_u, if lance geometry and weight are known. An alternative to using a point measurement of time-to-arrest or embedment-length, is to fit the recorded velocity history, to the rearranged Equation (A4) as

$$N'_q = \left[\arccos\left[\frac{\dot{x}'[t]}{U_0}\right]\frac{\sqrt{w}}{t}\right]^2 \tag{A10}$$

This enables N'_q, and hence S_u to be recovered from the deceleration history. Where the impact velocity, U_0, is significant, as $U_0 \gg [gw_b - N'_c]/n'_q\sqrt{N'_q/w}$, then the embedment history simplifies to

$$\dot{x}'[t] = U_0 \cos\left[\sqrt{\frac{N'_q}{w}}t\right] = U \tag{A11}$$

for velocity, and

$$x'[t] = U_0 \sqrt{\frac{w}{N'_q}} \sin\left[\sqrt{\frac{N'_q}{w}}t\right] \tag{A12}$$

for embedment depth.

APPENDIX B

Nomenclature

a	penetrometer radius, L
b	ratio of side adhesion to penetrometer mass, ST^{-1}
c	coefficient of consolidation, L^2T^{-1}
k	absolute permeability, L^2
N_c	dimensionless bearing capacity factor, —
N_D	dimensionless strength, —
P_D	dimensionless pressure, —
p	absolute pore fluid pressure, FL^{-2}
p_s	initial static fluid pressure, FL^{-2}

$p - p_s$	excess pore pressure, FL^{-2}
q_u	bearing capacity, FL^{-2}
R	radius of interest ($R^2 = x^2 + y^2 + z^2$), L
S_u	undrained cohesive strength, FL^{-2}
t	time (current), T
t_D	dimensionless time (current), —
t'_D	dimensionless time of penetrometer arrest, —
U	penetration rate, LT^{-1}
U_0	terminal velocity, LT^{-1}
U_D	dimensionless penetration rate, —
w	mass of penetrometer, $FL^{-1}T^2$
w_b	buoyant mass of penetrometer, $FL^{-1}T^2$
x_D, y_D, z_D	dimensionless Cartesian co-ordinates ($x/a; y/a; z/a$), —
x	location where the excess pore pressure is recorded, L
x'	distance below the seabed surface, L
ξ	dimensionless inverse root time ($\xi = R/\sqrt{c(t-\tau)}$), —
τ	time integrating parameter, —

ACKNOWLEDGEMENTS

This work is as a result of partial support from the National Science Foundation under grant CMS-04090002. This support is gratefully acknowledged. This paper has benefitted significantly from prior discussions with Miquel Canals and Roger Urgeles.

REFERENCES

1. Richards AF, Oien K, Keller GH, Lai JY. Differential piezometer probe for an *in situ* measurement of sea-floor pore-pressure. *Geotechnique* 1975; **25**(2):229–238.
2. Lee DR. A device for measuring seepage flux in lakes and estuaries. *Limnology and Oceanography* 1977; **22**(1): 140–147.
3. Harvey F, Rudolph DL, Frape SK. Measurement of hydraulic properties in deep lake sediments using a tethered pore pressure probe: applications in the Hamilton Harbour, western Lake Ontario. *Water Resources Research* 1997; **33**(8):1917–1928.
4. Schultheiss PJ, Noel M. Direct indication of pore water advection from pore pressure measurements in the Madeira Abyssal Plain sediments. *Nature* 1986; **320**:348–350.
5. Watts AB, Masson DG. A giant landslide on the north flank of Tenerife Canary Islands. *Journal of Geophysical Research* 1995; **100**(B4):24 487–24 498.
6. Torstensson BA. The pore pressure probe. *Nordiske Geotekniske Mote* 1977; **34**:34.1–34.15.
7. Robertson P, Campanella R, Gillespie D, Greig J. Use of piezometer cone data. *Proceedings of In Situ '86, American Society of Civil Engineers Speciality Conference*, GSP 6, New York, 1986; 1263–1280.
8. Levadoux JN, Baligh MM. Consolidation after undrained piezocone penetration. I: prediction. *Journal of the Geotechnical Engineering Division* (ASCE) 1986; **112**(7):707–726.
9. Baligh MM, Levadoux JN. Consolidation after undrained piezocone penetration. II: Interpretation. *Journal of the Geotechnical Engineering Division* (ASCE) 1986; **112**(7):727–745.
10. Robertson P, Sully J, Woeller D, Lunne T, Powell JM, Gillespie D. Estimating coefficient of consolidation from piezocone tests. *Canadian Geotechnical Journal* 1992; **29**(4):539–550.
11. Baligh, MM, Scott RF. Analysis of deep wedge penetration in clay. *Geotechnique* 1976; **26**(1):185–208.
12. Drescher A, Kang M. Kinematic approach to limit load for steady penetration in rigid-plastic soils. *Geotechnique* 1987; **37**(3):233–246.
13. Ladanyi B. Expansion of a cavity in a saturated clay medium. *Journal of the Soil Mechanics and Foundation Engineering Division* (ASCE) 1963; **89**(4):127–161.

14. Vesic A. Expansion of cavities in infinite soil mass. *Journal of the Soil Mechanics and Foundation Engineering Division* (ASCE) 1972; **98**:265–290.
15. Baligh MM. Strain path method. *Journal of the Geotechnical Engineering Division* (ASCE) 1985; **111**(9):1108–1136.
16. Acar Y, Tumay MT. Strain field around cones in steady penetration. *Journal of the Geotechnical Engineering Division* (ASCE) 1986; **112**(2):207–213.
17. Tumay MT, Acar YB, Cekirge MH, Ramesh N. Flow field around cone in steady penetration. *Journal of the Geotechnical Engineering Division* (ASCE) 1985; **111**(2):193–204.
18. Skempton AW. The pore pressure coefficients A and B. *Geotechnique* 1954; **4**(4):143–147.
19. Biot MA, Willis DG. The elastic coefficients of the theory of consolidation. *Journal of Applied Mechanics* 1957; **24**:594–601.
20. Davis EE, Horel GC, MacDonald RD, Villinger H, Bennett RH, Li H. Pore pressures and permeabilities measured in marine sediments with a tethered probe. *Journal of Geophysical Research* 1991; **96**(B4):5975–5984.
21. Fang WW, Langseth MG, Schultheiss PJ. Analysis and application of *in situ* pore pressure measurements in marine sediments. *Journal of Geophysical Research* 1993; **98**(B5):7921–7938.
22. Wang K, Davis EE. Theory for the propagation of tidally induced pore pressure variations in layered subseafloor formations. *Journal of Geophysical Research* 1996; **101**(B5):11483–11495.
23. Elsworth D. Analysis of piezocone data using dislocation based methods. *Journal of the Geotechnical Engineering Division* (ASCE) 1993; **119**(10):1601–1623.
24. Elsworth D. Indentation of a sharp penetrometer in a poroelastic medium. *International Journal of Solids and Structures* 1998; **35**(34–35):4895–4904.
25. Skempton AW. Cast-*in situ* bored piles in London clay. *Geotechnique* 1959; **9**:158.
26. Randolph M, Wroth C. An analytical solution for the consolidation around a driven pile. *International Journal of Numerical and Analytical Methods in Geomechanics* 1979; **3**:217–229.
27. Cleary MP. Fundamental solutions for a fluid-saturated porous solid. *International Journal of Solids and Structures* 1977; **13**(9): 785–806.
28. Elsworth D. Dislocation analysis of penetration in saturated porous media. *Journal of the Engineering Mechanics Division* (ASCE) 1991; **117**(2):391–408.
29. Mindlin RD. Force at a point in the interior of a semi-infinite solid. *Journal of Applied Physics* 1936; **7**(5):195–202.
30. Urgeles R, Canals M, Roberts J. SNV 'Las Palmas' Shipboard Party. Fluid flow from pore pressure measurements off La Palma, Canary Islands. *Journal of Volcanology and Geothermal Research* 2000; **101**:253–271.
31. Roberts J, Cramp A. Sediment stability on the western flanks of the Canary Islands. *Marine Geology* 1996; **134**: 13–30.
32. Elsworth D. Pore pressure response due to penetration through layered media. *International Journal of Numerical and Analytical Methods in Geomechanics* 1992; **16**(1):45–64.
33. Lee DS, Elsworth D. Indentation of a sharp penetrometer into a poroelastic seabed. *Journal of Engineering Mechanics* (ASCE) 2003; **130**(2):170–179.

